Supplement of Atmos. Chem. Phys., 18, 9879–9896, 2018
https://doi.org/10.5194/acp-18-9879-2018-supplement
© Author(s) 2018. This work is distributed under
the Creative Commons Attribution 4.0 License.

Atmospheric Chemistry and Physics
Open Access

Supplement of

Amplification of light absorption of black carbon associated with air pollution

Yuxuan Zhang et al.

Correspondence to: Qiang Zhang (qiangzhang@tsinghua.edu.cn)

The copyright of individual parts of the supplement might differ from the CC BY 4.0 License.

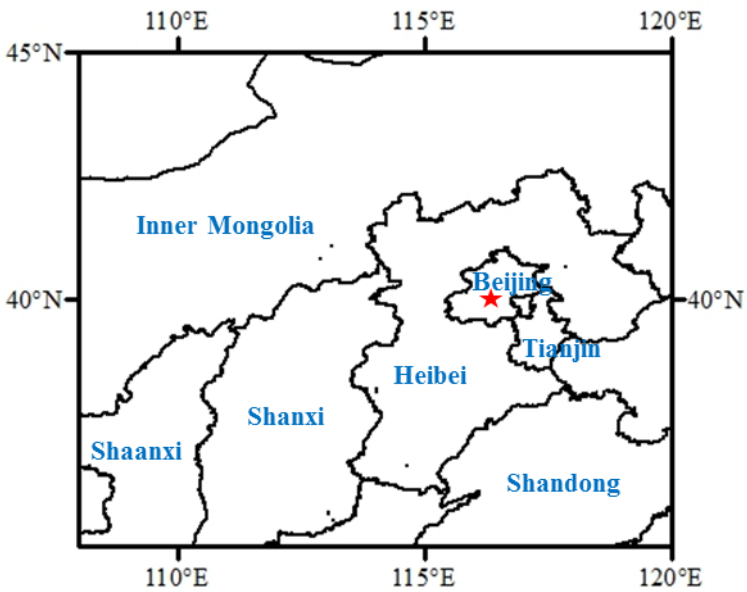

Figure S1. Location of the observation site (red star).

Figure S1 shows the geographic location of our observation site (namely red star marked in the Fig. S4). The site (40º00’17” N, 116º19’34” E) is located in megacity Beijing, the capital of China. The air pollution levels in our site can be influence by the air mass from adjacent regions (i.e., Tianjin, Heibei, Inner Mongolia, Shanxi, Shandong).

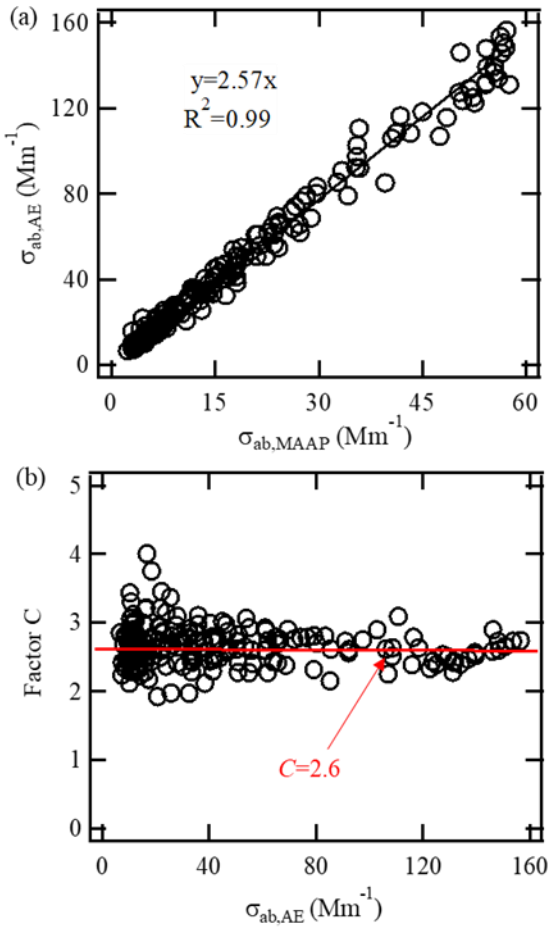

Figure S2. (a) The correlation between the absorption coefficient from AE33 at 660 nm ($\sigma_{ab,AE}$) and MAAP at 670 nm ($\sigma_{ab,MAAP}$). (b) Variety of multiple-scattering compensation factor *C* with different Aethalometer measurements.

Aethalometer artefacts are mainly from the loading effect and multiple-scattering effect (Weingartner et al., 2003; Segura et al., 2014). In terms of the loading effect, the compensation algorithm has been incorporated into Aethalometer model AE33 (Drinovec et al., 2015). In this study, we focused on the multiple-scattering compensation, which was characterized by enhancement parameter *C*. The factor *C* for our sites was determined by comparing the absorption coefficient derived from AE33 ($\sigma_{ab,AE}$) with the ones from MAAP ($\sigma_{ab,MAAP}$). Noted that the AE33 and MAAP measurements used to calculate the factor *C* were at different wavelengths, namely 660 nm and 670 nm, respectively. Considering that the absorption is inversely proportional to wavelength (Bond and Bergstrom, 2006), the difference in wavelength would lead to an uncertainty of ~1.5% for the corrected absorption coefficients in AE

measurement. As shown in Fig. S2a, the slope 2.6 was taken as the value of factor *C* to compensate the Aethalometer data. The specifically site-calculated values of the factor *C* varies in the range of 1.9-4 in this work (Fig. S2b), consistent with previous studies (Drinovec et al., 2015; Weingartner et al., 2003; Segura et al., 2014). In this study, the uncertainty in the factor *C* was dominated by the uncertainty in MAAP measurements. We corrected the MAAP data using the algorithm reported by Hyvärinen et al. (2013). They estimated that the uncertainty in absorption coefficients derived from MAAP based on the developed algorithm was ~15% by comparing the results from a PAS against those derived from the MAAP in Beijing. This indicated that the factor *C* used in our study (~2.6) would exhibit an uncertainty of ~15% from the uncertainty in MAAP measurements. Considering the uncertainty on the AE33 measurements was mainly from the factor *C*, the absorption coefficient from AE33 was estimated to have an uncertainty of ~15%.

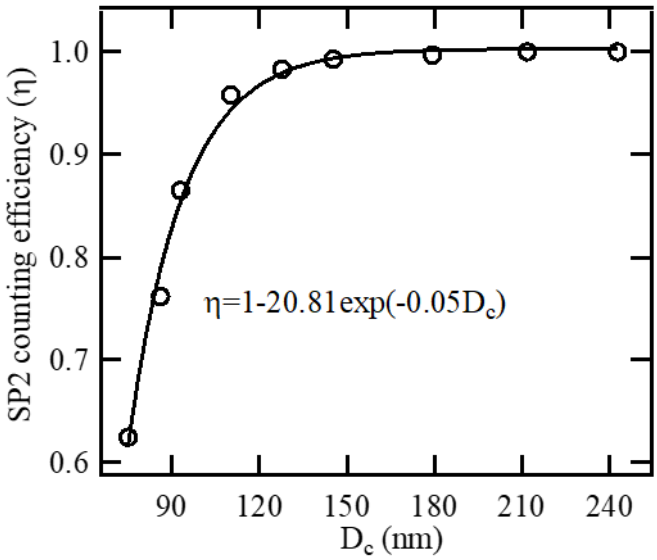

Figure S3. SP2 detection efficiency of particle (η) in each rBC size-bin.

Figure S3 shows the SP2 detection efficiency concentration (η) in each rBC size-bin. In our study, the SP2 detection efficiency was determined with a DMA-SP2/CPC system. Monodispersed Aquadag particles generated by DMA were simultaneously measured by SP2 and CPC. The size-resolved η was calculated by dividing the particle number concentration from SP2 measurement by that from CPC measurement. The SP2 detection efficiency (Fig. S3) have been considered in the

calculation of rBC mass concentration.

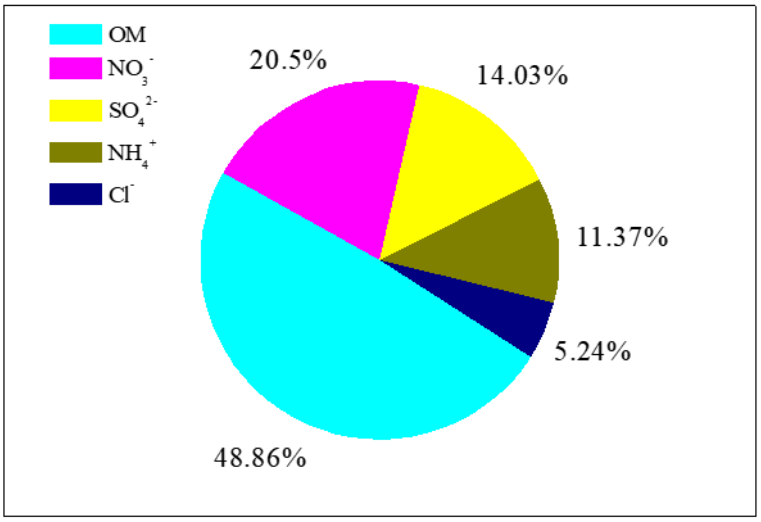

Figure. S4. Non-refractory compositions of PM_1 particles during the campaign period.

The RI_s value used in this study are 1.50-0i based on the chemical compositions of coating materials during the campaign period. The components of coating materials was similar to non-refractory compositions in PM_1 particles (Peng et al., 2016). Figure S4 reveals that the fraction of inorganic and organic components in coating materials of BC-containing particles are ~51% and ~49%, respectively. It is known from the literature (Schkolnik et al., 2007; Mallet et al., 2003; Marley et al., 2001) that major inorganic components of ambient aerosol from urban emission (nitrate, sulfate, mineral dust, sea salt and trace metal) have a refractory of (1.5-1.6)-0i and there is a range of (1.4-1.5)-0i for the refractory of organic components. In this study, we used the values of 1.55-0i and 1.45-0i as refractive indexes of inorganic and organic components of coating materials. The refractive index of a mixture particle can be calculated as the volume weighted average of the refractive indices of all components (Hänel, et al. 1968; Marley et al., 2001; Bond and Bergstrom, 2006; Schkolnik et al., 2007), as $\tilde{m} = \sum_i \tilde{m}_i c_i$, where $\tilde{m}$ is the refractive index of a mixture particle; $\tilde{m}_i$ is the refractive index of particle species; c is the volume ratio of particle species. Based on the equation, the refractive index of coating materials of BC-containing particles (RI_s) was ~1.50-0i during the campaign period.

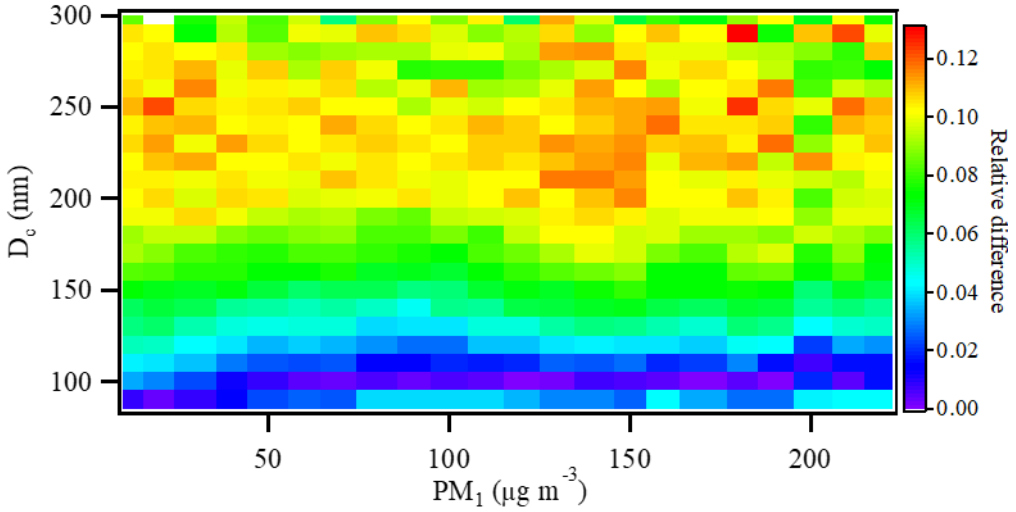

Figure S5. The relative difference between the sizes of BC-containing particles (D_p) derived from Mie calculation with RI_c of 2.26-1.26i and 1.95-0.79i.

Various values (e.g., 2.26-1.26i, 1.95-0.79i) of refractive index of BC core (RI_c) have be used in literature (Bond and Bergstrom, 2006; Cappa et al., 2012; Taylor et al., 2015). Figure S5 shows the relative difference between the sizes of BC-containing particles (D_p) derived from Mie calculation with RI_c of 2.26-1.26i and 1.95-0.79i. For BC-containing particles with 75-300 nm rBC cores, the relative difference is 3-10%, indicating that the D_p values were not sensitive to RI_c values in our study. This could be attributed to significantly larger in volume of coating materials than that of rBC cores.

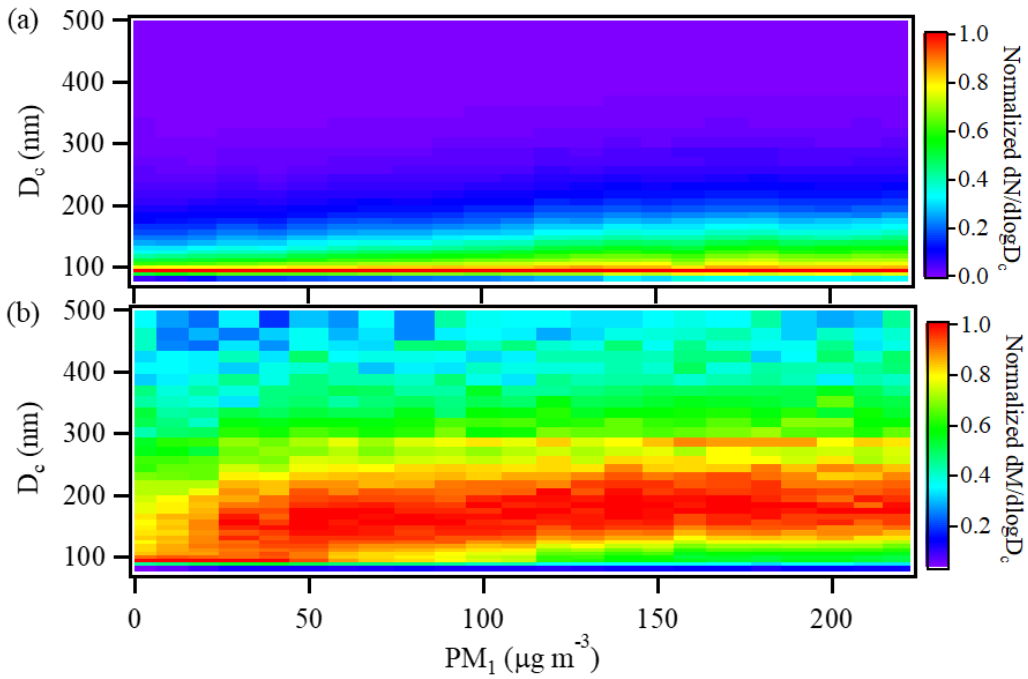

Figure S6. Size distribution of refractory BC (rBC) as a function of the PM_1 concentration: (a) number size distribution and (b) mass size distribution.

Figure S6 shows the size distribution of rBC as a function of the PM_1 concentration. Above the detection limit of SP2 incandescence (rBC with size larger than ~75 nm), the number size distribution of rBC cores shows a peak at ~95 nm under different PM_1 concentration (Fig. S6 (a)), and there are about 95% of rBC particles in number concentration lower than 200 nm. As shown in Fig. S6 (b)), the mass size distribution of rBC cores shows a wide mode at ~95-200 nm under different PM concentration.

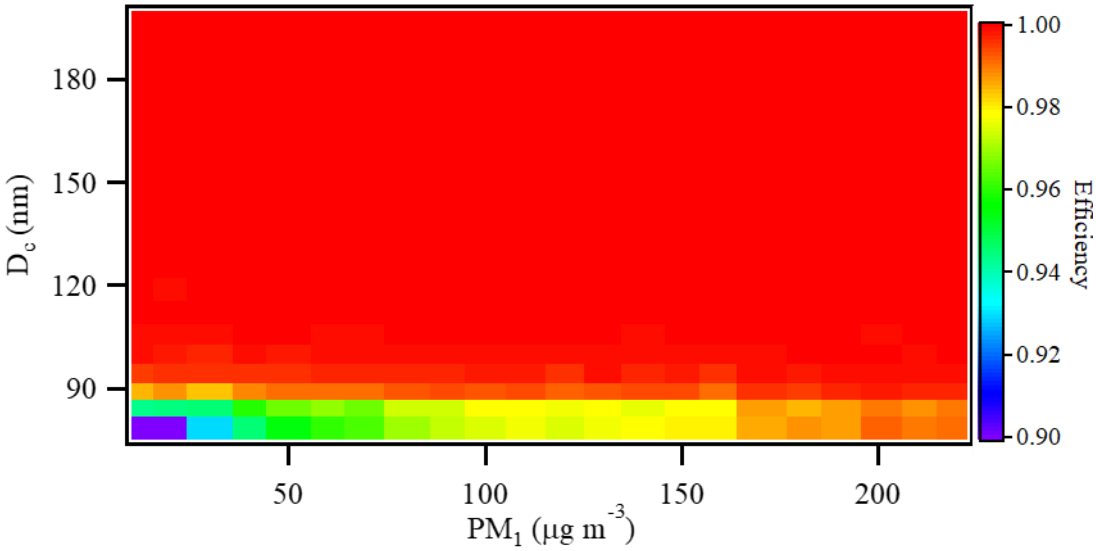

Figure S7. The detect efficiency of SP2 scattering for BC-containing particles with size-resolved rBC cores (75-200 nm) under different PM_1 concentration. In this study, the detect efficiency of SP2 scattering in terms of BC-containing particles at a certain rBC core size is defined as the ratio of the number concentration of particles above the detection limit of SP2 scattering and total particles.

Figure S7 shows the detect efficiency of SP2 scattering for BC-containing particles with size-resolved rBC cores (75-200 nm) under different PM_1 concentration. For BC-containing particles above the detection limit of our SP2 incandescence (rBC cores larger than ~75 nm), the detect efficiency of SP2 scattering is defined as the ratio of the number concentration of particles above the detection limit of SP2 scattering and total particles. The SP2 scattering exhibited a high detection efficiency (90-100%) for observed BC-containing particles with rBC cores more than 75 nm, which could be attributed to large BC-containing particles (~180-500 nm shown in Fig. S8) in our site due to atmospheric aging. High detection efficiency of SP2 scattering is favor to retrieve the thickness of coating materials on rBC cores (>75 nm size studied in this work) based on scattering signal.

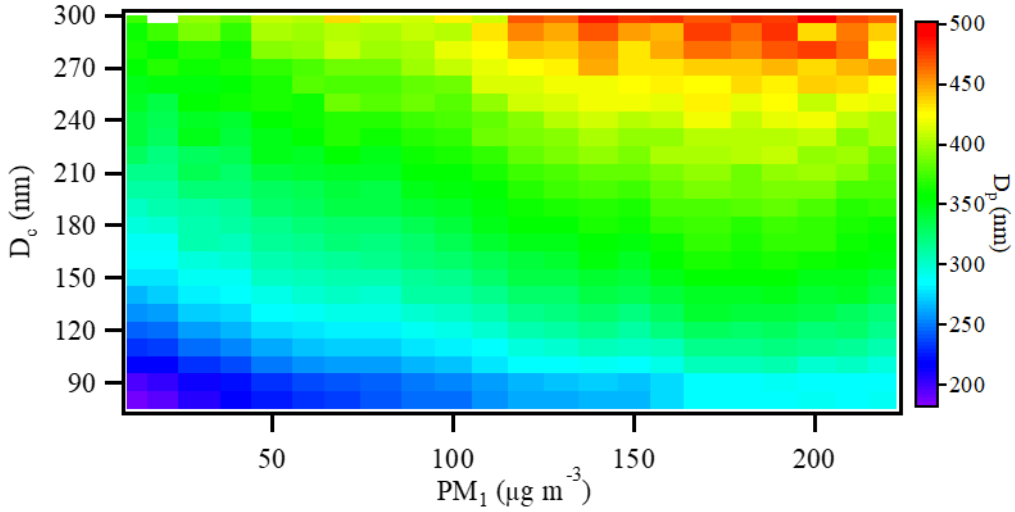

Figure S8. Frequency of the D_p/D_c ratio of BC-containing particles with size-resolved rBC cores as a function of PM1 concentrations.

Figure S8 shows frequency distribution of the D_p/D_c ratio of BC-containing particles with size-resolved rBC cores under different PM_1 concentrations. For BC-containing particles with 75-300 nm rBC cores, their particle size was in the range of 180-500 nm. The particle size (D_p) of BC-containing particles with rBC cores at a certain size significantly increased with increasing PM_1 concentration, revealing more coating materials on BC surface under more polluted environment.

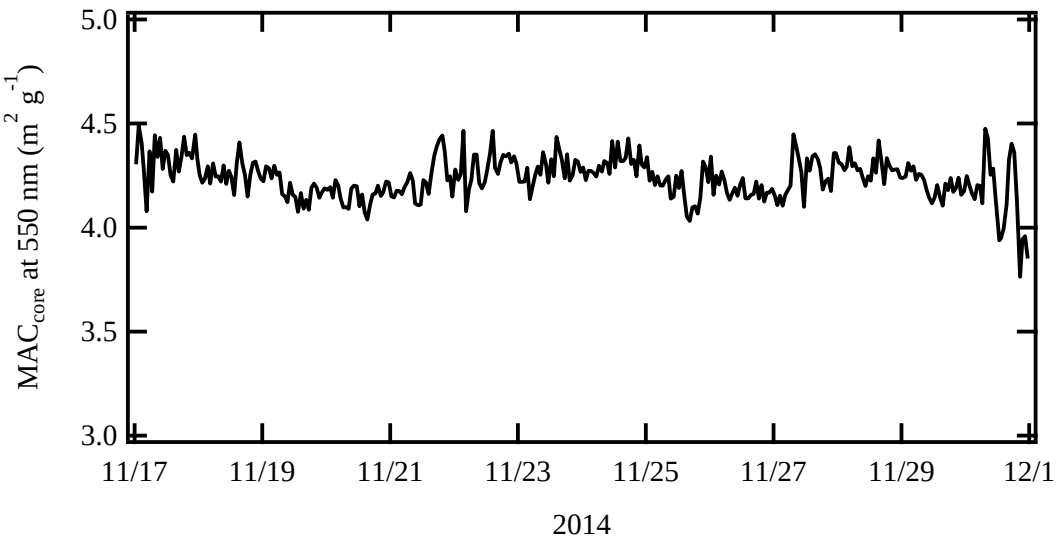

Figure. S9. The time series of MAC derived from Mie calculation for BC cores (i.e., bare BC) at 880 nm.

In this study, we used Mie mode to calculate optical properties of all

BC-containing particles including bare BC and aged BC. Note that Mie theory is fundamentally ill-suited to calculation of optical properties for bare BC particles, which would lead to an uncertainty of their light absorption. Based on Mie calculation, we obtained the *MAC* of rBC core (MAC_c) at 880 nm in the range of 3.8-4.5 m^2/g with an average of ~4.3 m^2/g during the campaign period (Fig. S9). Bond and Bergstrom (2006) suggested a value of 7.5 m^2/g for the MAC of bare BC at 550 nm. Considering that the absorption is inversely proportional to wavelength (Bond and Bergstrom, 2006), the MAC of bare rBC at 880 nm is estimated to be ~4.7 m^2/g, which was slightly greater than that (~4.3 m^2/g) obtained from Mie calculation in our study. This indicated the uncertainty of MAC for bare rBC from Mie calculation was ~8%. We estimated that the uncertainties of calculated BC light absorption related to MAC of bare rBC from Mie calculation was ~8%.

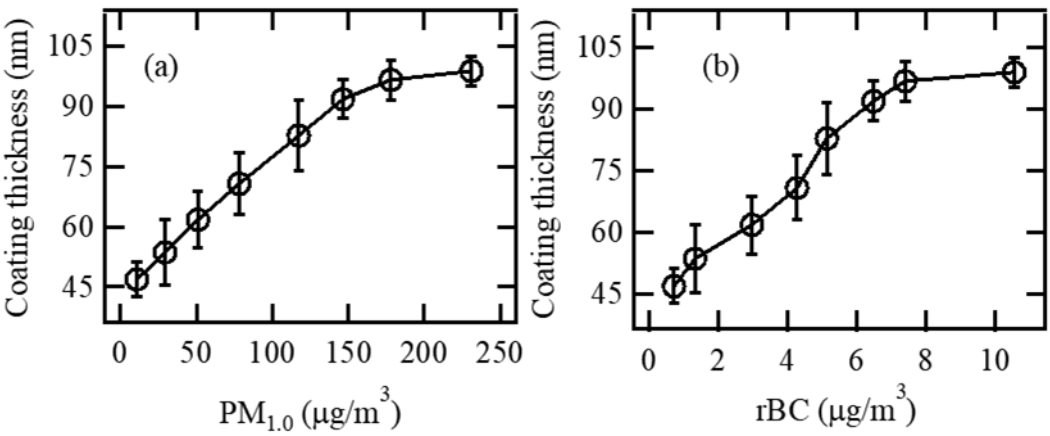

Figure S10. Variations in the coating thickness of BC-containing particles with the (a) PM_1 and (b) rBC mass concentrations.

Figure S10 shows the coating thickness of BC-containing particles increased with PM_1 and rBC concentration. The simultaneous increase in the rBC mass concentration and the amount of coating materials on the BC surface could significantly enhance the light absorption of BC-containing particles.

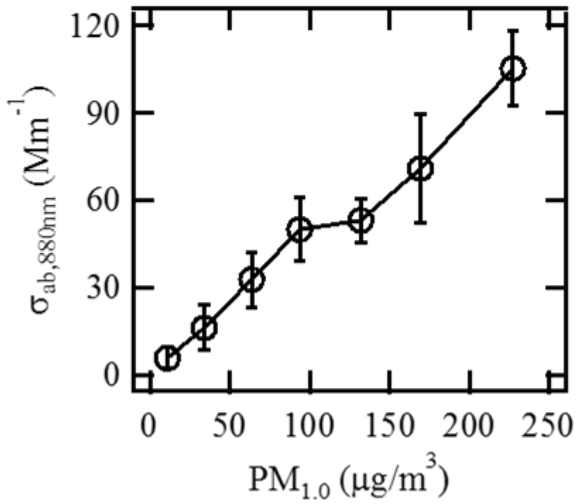

Figure S11. Changes of the light absorption coefficient at 880 nm ($\sigma_{ab,880nm}$) with PM_1 mass concentrations.

Figure S11 shows the changes of the light absorption coefficient at 880 nm ($\sigma_{ab,880nm}$) with PM_1 mass concentrations. The $\sigma_{ab,880nm}$ and rBC mass concentrations increased with increasing PM_1 mass concentrations. The simultaneous increase in the rBC mass concentration and the amount of coating materials shown in Fig. S10 revealed that the increase of $\sigma_{ab,880nm}$ (~18 fold from ~10 μg m^{-3} of PM_1 to ~230 μg m^{-3} of PM_1) could be attributed to simultaneous increase in the rBC mass concentration and the amount of coating materials on the BC surface.

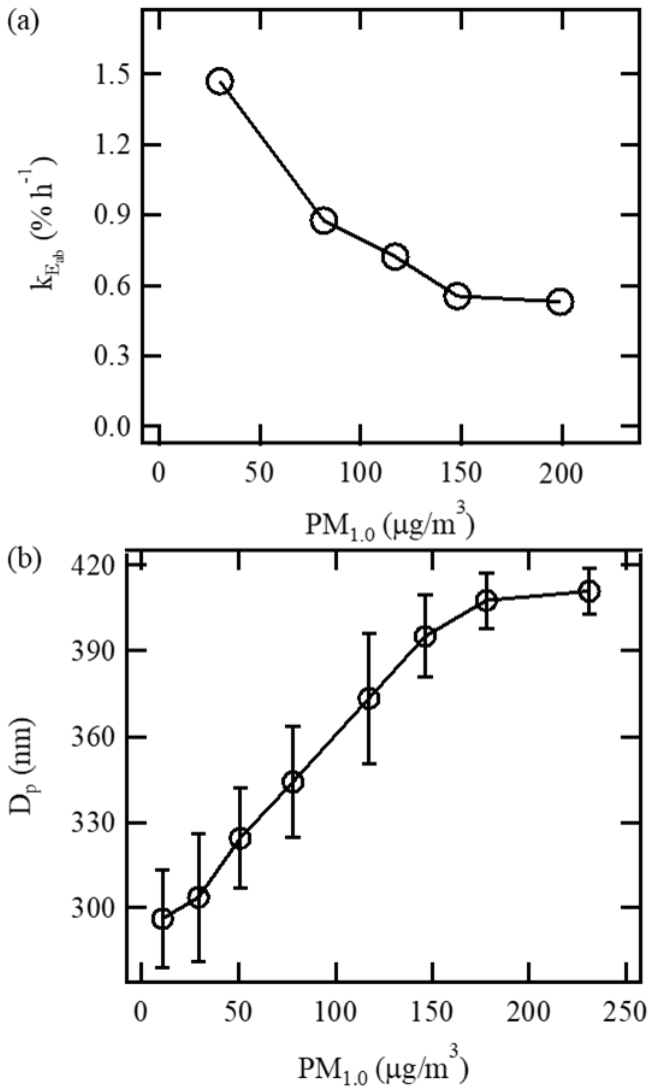

Figure S12. (a) Changes of growth rate of calculated E_{ab} (k_{Eab}) with PM_1 mass concentration. (b) Variations in the diameter of BC-containing particles (D_p) with the normalized PM_1 concentrations.

As shown in Figure S12, the changes of growth rate of E_{ab} (k_{Eab}) decreased with increasing PM_1 mass concentration. During the campaign period, the k_{Eab} of BC-containing particles was in the 0.5-1.5% h^{-1}. The decrease of k_{Eab} associated with air pollution indicated the enhancement of light absorption capability of BC-containing particles slowed with further air pollution, because BC aging process by condensational growth was less effective for more-aged BC particles with larger size under more pollution environment (Fig. S12b). The net change in diameter for a given amount of material deposited decreases with increasing particle size due to surface-to-volume scaling, which would expect the growth rate of particles to

decrease with increasing PM_1 concentration and thus the k_{Eab} would also decrease.

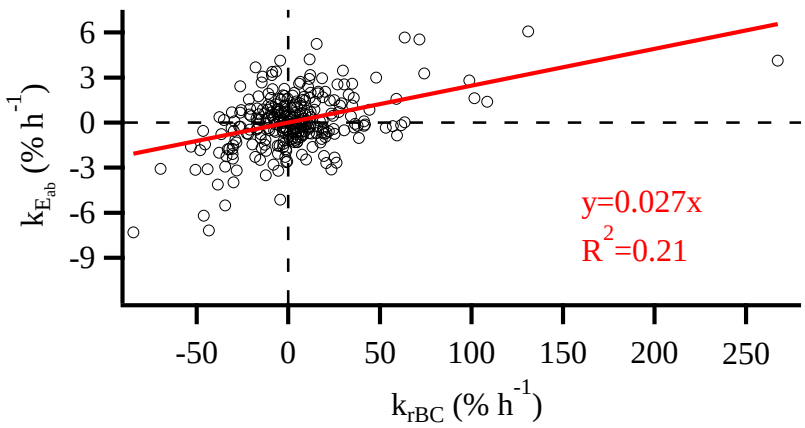

Figure S13. Correlation between the growth rate of E_{ab} (k_{Eab}) and the growth rates of rBC mass concentrations (k_{rBC}) during the campaign period.

Figure S13 shows the the relationship between the change rate of calculated E_{ab} (k_{Eab}) and the change rates of rBC mass concentrations (k_{rBC}) with pollution development. Linear relationships were estimated, i.e., $k_{Eab} \approx 0.027\ k_{rBC}$. Compared with the values of k_{rBC}, the significantly smaller k_{Eab} value indicated that the light absorption capability of BC increased more slowly than rBC mass concentrations.

Table S1 The DRF of externally mixed BC from global climate models. The modeled values were taken from Bond et al. (2013).

Global climate Model	Mixing state	Modeled MAC ($m^2\ g^{-1}$)	Modeled DRF ($W\ m^{-2}$)	Reference
AeroCom models				
GISS	External	8.4	0.22	Schulz et al. (2006)
LOA	External	8.0	0.32	Schulz et al. (2006)
LSCE	External	4.4	0.30	Schulz et al. (2006)
SPRINTARS	External	9.8	0.32	Schulz et al. (2006)
UIO-CTM	External	7.2	0.22	Schulz et al. (2006)
UMI	External	6.8	0.25	Schulz et al. (2006)
Other models				
BCC_AGCM	External	4.3	0.10	Zhang et al. (2012)
CAM3 ECA	External	10.6	0.57	Kim et al. (2008)
GISS-GCM II	External	7.8	0.51	Chung and Seinfeld (2002)
Average values		7.5	0.31	

The DRF values for BC-containing particles at different pollution levels were

obtained by scaling the average DRF (0.31 W m^{-2}) of externally mixed BC from various climate models (Bond et al. 2013) with a scaling factor of the calculated E_{ab} under different PM_1 concentrations (Fig. 2b). The DRF (0.31 W m^{-2}) of externally mixed BC was the global averages from the global climate models listed in Table S1. In order to point out the effect of BC light-absorption capability on DRF under different PM_1 concentrations, we did not consider the changes of BC amount for DRF calculation.

Table S2. Previous studies on the BC and PM (PM_1 or $PM_{2.5}$) mass concentrations in China.

Site	Measurement Period	PM (μg m^{-3})	BC (μg m^{-3})	Reference
Beijing (urban site)	1 to 31 January 2013	$PM_{2.5}$: ~4.4-855 (mean: 162)	~0.2-25	Zheng et al., 2015
Xi'an, Shaanxi (urban site)	23 December 2012 to 18 January 2013	$PM_{2.5}$: ~10-600	~0.3-44.5 (mean: 8.8)	Wang et al., 2014
Nanjing, Jiangsu (urban site)	1 January to 31 December 2015	PM_1: ~10-250 (mean: 48)	~0.5-20 (mean: 2.9)	Zhao et al., 2017
Shanghai (urban site)	5 to 10 December 2013	$PM_{2.5}$: ~40-636 (mean: 221)	~0.6-12.1 (mean: 3.2)	Gong et al., 2016
Jiaxing, Zhejiang (suburban site)	29 June to 15 July 2010 11 to 23 December 2010	PM_1: Summer ~4.6-104 (mean: 32.9) Winter 5.8-160 (mean: 41.9)	Summer ~0.4-11.7 (mean: 3.0) Winter ~0.52-49.5 (mean: 7.1)	Huang et al., 2013
Guangzhou, Guangdong (urban site)	5 October to 5 November 2004	$PM_{2.5}$: ~63-152 (mean:103)	~3-20 (mean:103)	Andreae et al., 2008
Heshan, Guangdong (suburban site)	From 21 November to 1 December 2010	$PM_{2.5}$: 23.5-145.2 (mean: 74.6)	2.9-13.8 (mean: 8.2)	Zhang et al., 2014

Table S2 lists the BC and PM (PM_1 or $PM_{2.5}$) mass concentrations in China in previous study. In this study, the PM_1 and rBC concentrations were 10-230 μg m^{-3} and 0.7-11 μg m^{-3} in Beijing during the campaign period (17 to 30 November 2014), which was consistent with previous studies in other polluted regions in China (Table S2). The consistency indicated that the enhancement of the light absorption capability of BC-containing particles associated with air pollution not only occurred in Beijing but also might be observed in other polluted regions in China.

References

Andreae, M. O., Schmid, O., Yang, H., Chand, D., Zhen Yu, J., Zeng, L.-M., and Zhang, Y.-H.: Optical properties and chemical composition of the atmospheric aerosol in urban Guangzhou, China, *Atmos. Environ.*, 42, 6335-6350, 2008.

Bond, T. C., and Bergstrom, R. W.: Light Absorption by Carbonaceous Particles: An Investigative Review, *Aerosol Sci. Technol.*, 40, 27-67, 2006.

Cappa, C. D., Onasch, T. B., Massoli, P., Worsnop, D. R., Bates, T. S., Cross, E. S., Davidovits, P., Hakala, J., Hayden, K. L., Jobson, B. T., Kolesar, K. R., Lack, D. A., Lerner, B. M., Li, S.-M., Mellon, D., Nuaaman, I., Olfert, J. S., Petäjä, T., Quinn, P. K., Song, C., Subramanian, R., Williams, E. J., and Zaveri, R. A.: Radiative Absorption Enhancements Due to the Mixing State of Atmospheric Black Carbon, *Science*, 337, 1078-1081, 2012.

Chung, S. H., and Seinfeld, J. H.: Global distribution and climate forcing of carbonaceous aerosols, *J. Geophys. Res.-Atmos.*, 107, AAC 14-11-AAC 14-33, 10.1029/2001JD001397, 2002.

Drinovec, L., Močnik, G., Zotter, P., Prévôt, A., Ruckstuhl, C., Coz, E., Rupakheti, M., Sciare, J., Müller, T., and Wiedensohler, A.: The" dual-spot" Aethalometer: an improved measurement of aerosol black carbon with real-time loading compensation, *Atmos. Meas. Tech.*, 8, 1965-1979, 2015.

Gong, X., Zhang, C., Chen, H., Nizkorodov, S. A., Chen, J., and Yang, X.: Size distribution and mixing state of black carbon particles during a heavy air pollution episode in Shanghai, Atmos. Chem. Phys., 16, 5399-5411, 2016.

Hänel, G.: The real part of the mean complex refractive index and the mean density of samples of atmospheric aerosol particles, *Tellus*, 20, 371-379, 1968.

Huang, X.-F., Xue, L., Tian, X.-D., Shao, W.-W., Sun, T.-L., Gong, Z.-H., Ju, W.-W., Jiang, B., Hu, M., and He, L.-Y.: Highly time-resolved carbonaceous aerosol characterization in Yangtze River Delta of China: Composition, mixing state and secondary formation, *Atmos. Environ.*, 64, 200-207, 2013.

Hyvärinen, A.-P., Vakkari, V., Laakso, L., Hooda, R. K., Sharma, V. P., Panwar, T. S., Beukes, J. P., van Zyl, P. G., Josipovic, M., Garland, R. M., Andreae, M. O., Pöschl, U., and Petzold, A.: Correction for a measurement artifact of the Multi-Angle Absorption Photometer (MAAP) at high black carbon mass concentration levels, *Atmos. Meas. Tech.*, 6, 81-90, 2013.

Kim, D., Wang, C., Ekman, A. M. L., Barth, M. C., and Rasch, P. J.: Distribution and direct radiative forcing of carbonaceous and sulfate aerosols in an interactive size-resolving aerosol–climate model, *J. Geophys. Res.-Atmos.*, 113, 10.1029/2007JD009756, 2008.

Mallet, M., J.C. Roger, S. Despiau, O. Dubovik and J.P. Putaud (2003), Microphysical and optical properties of aerosol particles in urban zone during ESCOMPTE. *Atmos. Res.*, 69(1-2), 73-97.

Marley, N.A., J.S. Gaffney, C. Baird, C.A. Blazer, P. J. Drayton and J. E. Frederick (2001), An empirical method for the determination of the complex refractive index of size fractionated atmospheric aerosols for radiative transfer calculations, *Aerospace. Sci. Technol.* 34(6), 535-549.

Schkolnik, G., D. Chand, A. Hoffer, M.O. Andreae, C. Erlick, E. Swietlicki and Y. Rudich (2007), Constraining the density and complex refractive index of elemental and organic carbon in biomass burning aerosol using optical and chemical measurements, *Atmos. Environ*., 41, 1107-1118.

Schulz, M., Textor, C., Kinne, S., Balkanski, Y., Bauer, S., Berntsen, T., Berglen, T., Boucher, O., Dentener, F., Guibert, S., Isaksen, I. S. A., Iversen, T., Koch, D., Kirkevåg, A., Liu, X., Montanaro, V., Myhre, G., Penner, J. E., Pitari, G., Reddy, S., Seland, Ø., Stier, P., and Takemura, T.: Radiative forcing by aerosols as derived from

the AeroCom present-day and pre-industrial simulations, *Atmos. Chem. Phys*., 6, 5225-5246, 2006.

Segura, S., Estellés, V., Titos, G., Lyamani, H., Utrillas, M. P., Zotter, P., Prévôt, A. S. H., Moˇcnik, G., Alados-Arboledas, L., and Martínez-Lozano, J. A.: Determination and analysis of in situ spectral aerosol optical properties by a multi-instrumental approach, *Atmos. Meas. Tech*., 7, 2373–2387, 2014.

Taylor, J. W., Allan, J. D., Liu, D., Flynn, M., Weber, R., Zhang, X., Lefer, B. L., Grossberg, N., Flynn, J., and Coe, H.: Assessment of the sensitivity of core / shell parameters derived using the single-particle soot photometer to density and refractive index, *Atmos. Meas. Tech*., 8, 1701-1718, 2015.

Wang, Q., Huang, R. J., Cao, J., Han, Y., Wang, G., Li, G., Wang, Y., Dai, W., Zhang, R., and Zhou, Y.: Mixing State of Black Carbon Aerosol in a Heavily Polluted Urban Area of China: Implications for Light Absorption Enhancement, *Aerosol Sci. Technol.*, 48, 689-697, 2014.

Weingartner, E., Saathoff, H., Schnaiter, M., Streit, N., Bitnar, B., and Baltensperger, U.: Absorption of light by soot particles: determination of the absorption coefficient by means of aethalometers, *J. Aerosol Sci.*, 34, 1445–1463, 2003.

Zhang, G., Bi, X., He, J., Chen, D., Chan, L. Y., Xie, G., Wang, X., Sheng, G., Fu, J., and Zhou, Z.: Variation of secondary coatings associated with elemental carbon by single particle analysis, *Atmos. Environ.*, 92, 162-170, 2014.

Zhang, H., Wang, Z., Wang, Z., Liu, Q., Gong, S., Zhang, X., Shen, Z., Lu, P., Wei, X., Che, H., and Li, L.: Simulation of direct radiative forcing of aerosols and their effects on East Asian climate using an interactive AGCM-aerosol coupled system, *Clim. Dyn*., 38, 1675-1693, 10.1007/s00382-011-1131-0, 2012.

Zhao, Q., Shen, G., Li, L., Chen, F., Qiao, Y., Li, C., Liu, Q., and Han, J.: Ambient Particles (PM10, PM2.5 and PM1.0) and PM2.5 Chemical Components in Western Yangtze River Delta (YRD): An Overview of Data from 1-year Online Continuous Monitoring at Nanjing, *Aerosol Sci. Eng.*, 2017.

Zheng, G. J., Duan, F. K., Su, H., Ma, Y. L., Cheng, Y., Zheng, B., Zhang, Q., Huang, T., Kimoto, T., Chang, D., Pöschl, U., Cheng, Y. F., and He, K. B.: Exploring the

severe winter haze in Beijing: the impact of synoptic weather, regional transport and heterogeneous reactions, *Atmos. Chem. Phys.*, 15, 2969-2983, 2015.